

Variability in the South Pacific Deep Western Boundary Current from current meter observations and a high-resolution global model

Mike I. Moore¹

National Institute for Water and Atmospheric Research, Wellington, New Zealand

John L. Wilkin²

CSIRO Division of Marine Research, Hobart, Tasmania, Australia

Abstract. Observations of the South Pacific Deep Western Boundary Current from the World Ocean Circulation Experiment Pacific current meter array 9 (WOCE PCM-9) current meter array are compared with the Los Alamos National Laboratory high-resolution global ocean model. A simple integration of PCM-9 velocity yields a mean northward transport of water deeper than 3000 m that is some 5 times greater than the model mean transport of $3.35 \times 10^6 \text{ m}^3 \text{ s}^{-1}$. The low modeled abyssal transport suggests a poor simulation of the mean thermohaline circulation. However, model and observed transport variability correlate significantly. Space-time spectral analysis shows planetary waves are responsible for most of the variability and are resolved well in the model. The details of interaction of the long waves at the western boundary are different in model and data. The model reflects these waves predominantly as planetary short waves, which decay over the region 600–800 km east of the Kermadec Ridge. PCM-9 has a higher proportion of energy as topographic waves along the Kermadec Ridge. These two classes of waves are associated with the two observed zonal scales in the boundary current. The model results can be separated into vertical modes. Baroclinic energy is found at all timescales, including those too short for free baroclinic waves. The baroclinic flow correlates with the barotropic so as to enhance surface, and reduce abyssal, kinetic energy. This is the signature of planetary wave scattering at the submerged western boundary ridge, and results in enhanced baroclinic wave energy in the Tasman Sea.

1. Introduction

Circumpolar Deep Water enters the abyssal Pacific as a western-intensified stream along the boundary formed by the New Zealand continental slope and the Kermadec Ridge. This is as expected from the abyssal circulation theory of *Stommel and Arons* [1960] and was first observed directly in the 1960s [e.g., *Reid et al.*, 1968; *Warren*, 1970]. In a hydrographic section along 28°S, *Warren* [1970] found a boundary current extending 900 km east from the Kermadec Ridge transporting $17 \times 10^6 \text{ m}^3 \text{ s}^{-1}$ of water deeper than 2500 m. Since this work, until the advent of the World Ocean Circulation Experiment (WOCE), there were no further observations of the South Pacific Deep Western Boundary Current (DWBC). As part of the thermohaline circulation, this flow is important in the exchange of heat and salt between the Southern and Pacific Oceans. To reduce uncertainty in the flux terms in this balance, WOCE programs have devoted considerable effort to observing the South Pacific DWBC, including basin-wide hydrographic sections at 32°S (the WOCE P-6 transect), and Pacific current

meter (PCM) arrays at Samoa Passage [*Roemmich et al.*, 1996] and at 32.5°S: the WOCE “PCM-9” array.

The PCM-9 array was deployed from February 1991 to November 1992 in a 1000 km line east of the Kermadec Ridge [*Nowlin and Whitworth*, 1991; *Moore and Chiswell*, 1993; *Pillsbury et al.*, 1994] (Figure 1).

Conductivity-temperature-depth (CTD) surveys made during the period are described by *Moore et al.* [1993], *Moore* [1994], *Whitworth et al.* [1995], and S. Wijffels and J. Toole (unpublished manuscript, 1997). The primary goal of the PCM-9 project, namely, to measure the mean transport of the DWBC, is the subject of the work by T. Whitworth et al. (On the deep western boundary current in the Southwest Pacific Basin (submitted to *Progress in Oceanography*, 1997; hereinafter referred to as submitted paper). Our interest is to determine the dynamic processes producing the large variability in velocity observed by the array at periods from a few days to several months.

The simplest dynamic hypothesis is that observed variability is the result of free planetary waves, probably with some degree of topographic influence. This is anticipated from the role of planetary waves in western intensification. Moreover, recent satellite altimeter observations show the importance of persistent, coherent waves in low-latitude and midlatitude variability [*Jacobs et al.*, 1994; *Chelton and Schlax*, 1996]. The 1000-km length of the PCM-9 array provides an opportunity to observe the zonal phase propagation of such waves.

¹Now at New Zealand Dairy Board, Wellington.

²Now at School of Environmental and Marine Sciences, University of Auckland, Auckland, New Zealand.

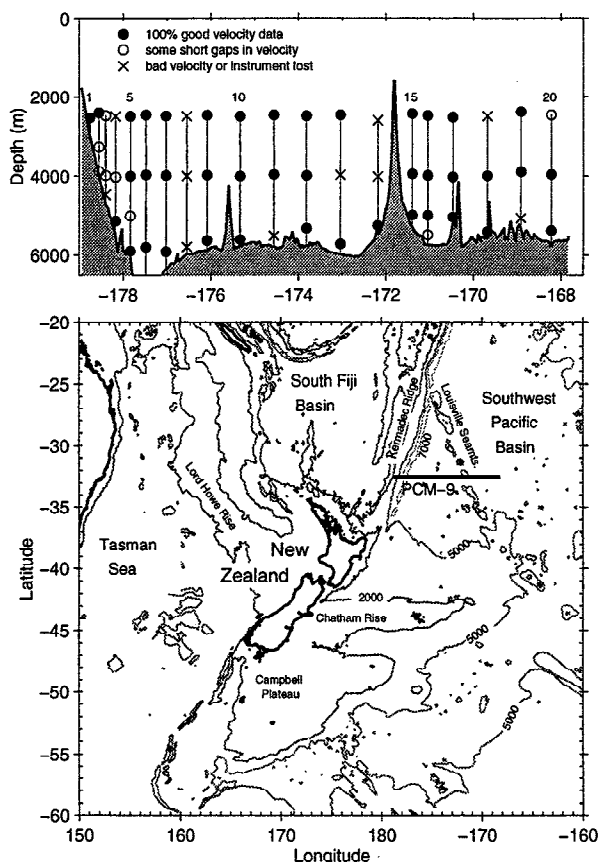


Figure 1. PCM-9 current-meter array and regional bathymetry. The only serious data gap is an 11% data loss (days 325–398, 1991) at mooring 3, 2500 m. This gap was filled by interpolation between moorings 2 and 4. All other gaps were filled by interpolation within the time series.

We find evidence that planetary and topographic waves account for most of the variability in the abyssal transport at PCM-9. Significant temporal correlation between the observed variability and that simulated in a high-resolution global model driven with observed winds proves the model is a suitable tool for inferring the role of planetary waves in ocean variability across a range of Pacific longitudes that would be impractical to observe directly.

2. Combination of Observations and a Model

The previously observed width of the DWBC meant that PCM-9 had to be a very large undertaking, using 20 moorings with an average of three current meters each. One consequence was that current meters were not placed shallower than the expected depth of the DWBC and the array cannot resolve variability into vertical modes. Also, although 1000 km is long for an array of current meters, it is short compared to the zonal scale of planetary long waves which we postulate reflect into short waves at the Kermadec Ridge. To overcome these limitations on spatial scope of the array, we use results from the Los Alamos National Laboratory (LANL) global ocean model. This model is similar to the familiar Bryan-Cox-Semtner code but with modifications to improve performance on massively parallel computers [Dukowicz and Smith, 1994].

The model has 20 vertical levels and uses a horizontal grid with resolution 0.28° longitude by $\cos(\text{lat}) \times 0.28^\circ$ latitude.

Along 32.5°S the grid spacing is therefore 26.4 km. The model was initialized from the results of a similar 0.4° resolution model [Stammer *et al.*, 1996] and then integrated for a 10-year period from January 1985 using 3-day averages of European Center for Medium-Range Weather Forecasting (ECMWF) analyses for the surface wind stress (M. E. Maltrud *et al.*, Global eddy-resolving ocean simulations driven by 1985–1994 atmospheric winds, submitted to *Journal of Geophysical Research*, 1997). Surface heat and freshwater fluxes were parameterized by relaxing model surface temperature and salinity to a monthly climatology. The LANL group archived a subset of results from the model integration in anticipation of the analysis presented here. Model velocity was interpolated horizontally to the coordinates of the PCM-9 moorings and archived daily for all model levels. In addition, snapshots of model results were archived at all grid points along 32.5°S every 3 days of the 10-year run.

This archiving procedure potentially aliases internal gravity waves. However, the LANL model applies a gravity wave filter in order to extend the allowable time step. This, in combination with no forcing at less than 3-day timescales, means we expect little or no gravity wave energy in the model. In fact, we find the model has little energy on timescales shorter than 10 days. We therefore choose to 10-day low-pass filter both model and data for the purposes of comparison.

In order to use the model to augment the PCM-9 data, we require confidence that model and observations exhibit sufficiently similar variability in the PCM-9 region that the model may be trusted as indicative of unobserved flows adjacent to PCM-9 and right across the Pacific. We make this comparison in some detail because it will provide insights into what processes are resolved well, or poorly, in the model.

We will show that the model underestimates the mean strength of the DWBC, with the possible implication of a poor simulation of the mean thermohaline circulation. This is not surprising; a model integration time of 10 years is insufficient to allow diabatic processes to come into equilibrium. Despite this shortcoming, there is a clear temporal correlation between observed and modeled abyssal transport at timescales resolved by the PCM-9 deployment. This suggests that the dynamics of the observed and modeled variability are similar, which is an expected result if the variability is due to adiabatic dynamics that should be simulated well by a high-resolution global primitive equation model with realistic wind forcing. Having established this dynamical correspondence, we use the model to extend our view of the Pacific, vertically, horizontally and temporally, beyond the limits of the PCM-9 array.

3. Observed and Modeled Mean Circulation

3.1. Mean Velocity

Figure 2 shows the mean velocity from PCM-9 and the model for the array deployment period. The PCM-9 data show a strong, narrow cell of northward flow confined within about 1° longitude of the Kermadec Ridge, and extending from the bottom to the shallowest metered level of 2500 m. This jet is most intense near the bottom, where mean velocity peaks at 7.9 cm s^{-1} . A clear recirculation feature is seen just to the east, over the Kermadec Trench, where mean velocity peaks at -1.9 cm s^{-1} at 4000 m. The PCM-9 data are faintly suggestive of a second, bottom-intensified, northward core east of the Louisville Seamounts. However, the loss of three instruments just

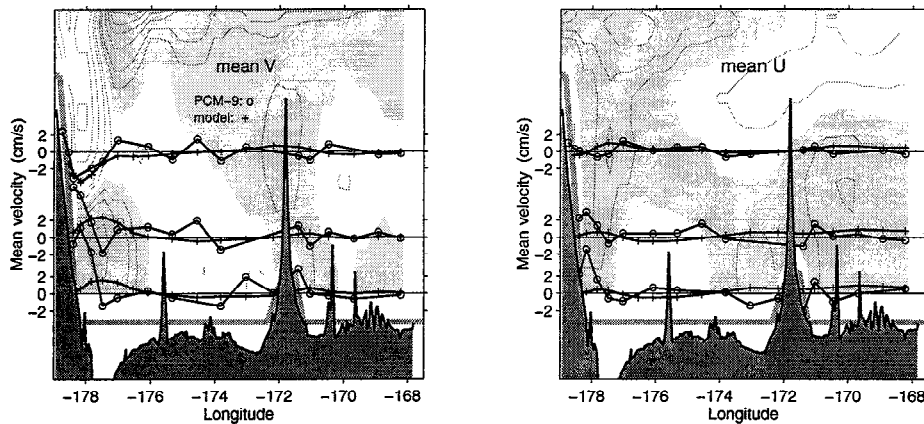


Figure 2. Mean meridional and zonal velocity (v and u , respectively) in model and data. Model levels of 2475, 4125, and 5000 m are compared with nominal 2500 m, 4000 m, and near-bottom levels in PCM-9. The model velocity at other depths is also shown by the contours (at 1 cm s^{-1} intervals, shaded where positive). Shaded bathymetry is as observed on the deployment cruise. Model bathymetry is the broad grey line. The Kermadec Ridge is at left, the Kermadec Trench is immediately east, and the Louisville Seamount Chain is at 172°W . The other features are isolated seamounts (see Figure 1).

west of the Louisville Seamounts (Figure 1) makes it difficult to be sure of the significance of this feature.

The model shows a broader and smoother zonal variation of meridional velocity, and there is no recirculation over the Kermadec Trench (which is absent from the model bathymetry). Rather, the strong core of southward flow at 2500 m penetrates more deeply than observed in hydrographic sections [e.g., Reid *et al.*, 1968], in apparent negation of the DWBC. This core is part of a model boundary current against the Kermadec Ridge that transports intermediate depth waters southward from Samoa to the Chatham Rise but appears to be too strong and too deep in the model (L. Carter and J. Wilkin, unpublished manuscript, 1997). The model shows a minor, secondary intensification of the northward flow at the Louisville Seamounts, even though the seamounts are small in the model. This may be a result of the abyssal flow following topographic features much more faithfully than in reality.

With the exception of the southward boundary current, the model mean velocity is weaker than in the data. Northward flow peaks at 2.7 cm s^{-1} at 4125-m depth east of Kermadec Ridge, and 0.68 cm s^{-1} at 5000 m east of the Louisville Seamounts. The recirculation velocities are also weaker with peak mean velocity -0.43 cm s^{-1} at 4125-m depth. This is a much broader feature than in the data, being most apparent at about 175°W .

Whereas the observed velocity peaks either at the first mooring, or no more than 20 km from the ridge, the model current is zero at the ridge, falling from its peak value in a boundary layer more than 100 km wide. This is a frictional boundary layer required by the no-slip condition imposed at the bathymetry. Evidently, the frictional dissipation is too strong, and peak velocities are well below those observed.

The immediate impression is that the data have a narrow, 90-km scale, western boundary current and that the model has a broader, 200-km zonal scale, though this is still narrower than Warren's [1970] 900 km. However, a larger scale is more evident in PCM-9 when we plot abyssal transport as a cumulative function of distance eastward from the Kermadec Ridge (Figure 3). We compute the abyssal transports by integrating below two choices of cutoff depth: 2000 and 3000 m. The deeper level avoids the anomalous southward intermediate-depth boundary current in the model but has little effect on the PCM-9 calculation.

The strong core in the far west of the PCM-9 data is responsible for about 10 Sv ($1 \text{ Sv} = 1 \times 10^6 \text{ m}^3 \text{ s}^{-1}$) transport over only 90 km (basically confined to the slope of the ridge), but a further 10 Sv is achieved below 2000 m by a broader flow extending 600–800 km from the Kermadec Ridge.

The model accumulates most of its northward transport deeper than 3000 m within 200 km of the Kermadec Ridge,

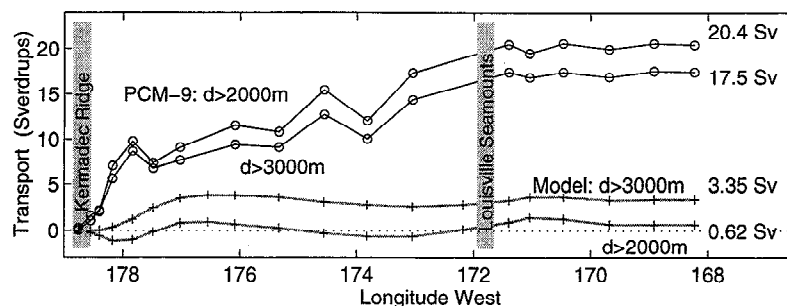


Figure 3. Cumulative transport eastward from mooring 1 (Kermadec Ridge) calculated by integrating meridional velocity from depths 2000 and 3000 m to the seafloor.

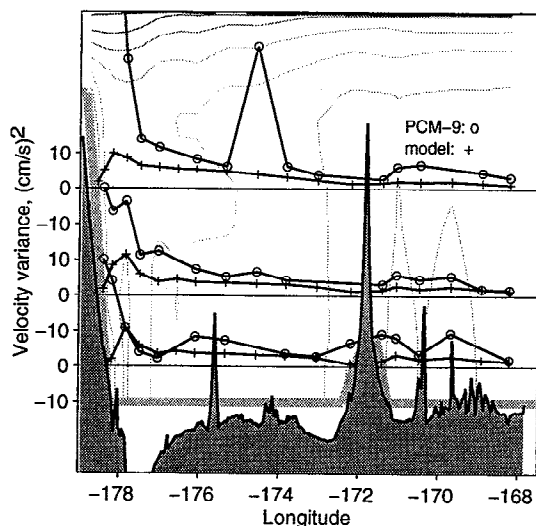


Figure 4. Observed and modeled velocity variance. The isolated peak at 174°W, 2500-m depth, in the observations is the result of a single very intense burst of northward flow that is unexplained yet thought to be real, partly because it appears in a reduced form at 4000 m.

with no additional accumulation on the larger space scale seen in PCM-9. There is a hint of a similar 200-km scale east of the Louisville Seamounts. Despite the influence of the anomalous southward intermediate flow, the same zonal scales are seen in the model transport deeper than 2000 m.

Our total PCM-9 transport is greater than the 13.6 Sv estimated by T. Whitworth et al. (submitted paper, 1997), in an analysis that takes account of vertical shear at adjacent moorings to help fill missing current meter records. However, a sensitive analysis is not required to expose the fivefold discrepancy in modeled and observed transport. The estimate of the transport we use is adequate for the goals of this paper: to assess variability, and to compare observations with the LANL model.

Thus the model does not properly resolve the DWBC core, has an unrealistic frictional boundary layer, does not exhibit the zonal scales of the observed DWBC, and has a total transport that is some 5 times too low compared to any estimate of PCM-9.

3.2. Kinetic Energy

East of the Kermadec Trench, velocity variance (mean eddy kinetic energy) decays toward the east, with comparable magnitude and length scale (600–800 km) in model and data (Figure 4). Near the Kermadec Ridge the energy level in PCM-9 rises rapidly and is maximum closest to the ridge. This high-energy region spans about 1° longitude at 2500 m, similar to the scale of the western core of the mean flow in PCM-9 and its recirculation. The peak energy level falls from $165 \text{ cm}^2 \text{ s}^{-2}$ at 2500 m to $30 \text{ cm}^2 \text{ s}^{-2}$ at the foot of the ridge, but the width of the high-energy region does not broaden, whereas the core of mean flow does (Figure 2). Peak energy values for the model are lower and take a maximum some 100 km eastward of the ridge, dropping to zero against the ridge, consistent with the model no-slip boundary condition. This difference in peak energy may be further evidence that the model is overly dissipative in the boundary layer, or that it poorly simulates the topographic influence of the ridge and trench.

The similarity of the larger length scale in observed and modeled velocity variance, and the dissimilarity of the smaller scale, begs the question: what are the dynamical processes in the observed and modeled variability?

4. Observed and Modeled Variability

A typical comparison between velocity time series from PCM-9 and the model is shown in Figure 5 for the meridional component at mooring 5. There is a small amount of event-to-event correspondence, but the comparison is lackluster, and coherences (not shown) are generally low. Moreover, the model shows considerably less vertical shear than the data.

Time series of total transport compare more favorably. Figure 6 shows the transports integrated across the array region for depths below 2000 m. (The variability series are little affected if 3000 m is used as the upper limit.) Although the mean transport in the model is low, the standard deviation of the model transport, 8.2 Sv, is much closer to the observed 13.6 Sv. The two time series show considerable eventwise correspondence, though with a variable lag/lead relationship. For example, compare the events at days 130–150 and 380–410. Figure 6 shows coherence and phase spectra between the model and observed transports computed by standard periodogram smoothing [e.g., Koopmans, 1974, equations (8.51)–(8.54); Priestley, 1981, equations (9.5.8), (9.5.14)]. A triangular spectral window with five points was used, giving 8.5 equivalent degrees of freedom [e.g., Koopmans, 1974, (8.39); Priestley, 1981, p. 396, 466, 467]. Confidence intervals at the 90% level are shown [e.g., Priestley, 1981, equations (9.5.48), (9.5.54), (9.5.27)]. Coherence is significant, except for a large gap at 33–50 days and a smaller one at 18–20 days. The phase spectrum shows up to an 8-day lead of the model transport series relative to PCM-9, at a period of 100 days, but from inspection of the time series this is a variable relationship. This phase variability has probably reduced the coherences, since all such spectral analyses assume stationarity in the data. The model lead of a few days would be consistent with the model rigid lid approximation, causing the propagation speed for planetary waves to be slightly overestimated, thereby communicating the effects of remote forcing too rapidly to the boundary.

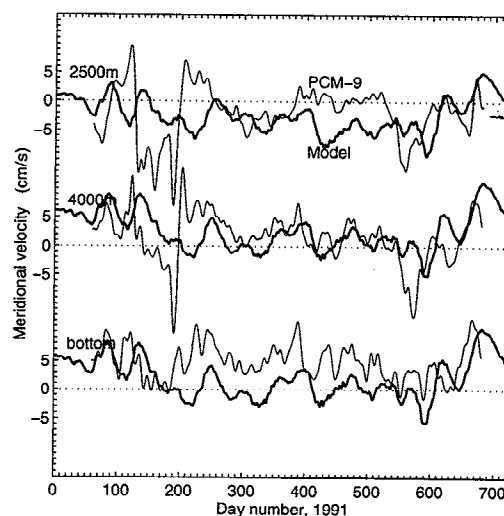


Figure 5. Mooring 5 meridional velocity time series. The comparison is typical of modeled and observed velocity.

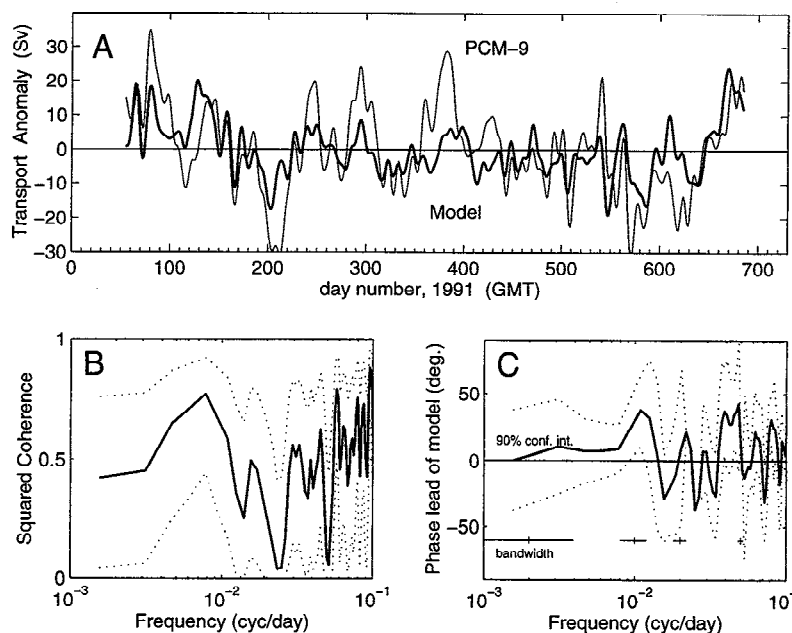


Figure 6. Abyssal transport integrated from 2000 m to the bottom and across the extent of PCM-9: (a) time series, (b) squared coherence, and (c) phase. The bandwidth of independent spectral estimates of coherence is the same as shown for phase.

It is clear that the variability is modeled considerably better than the mean transport. The low model mean abyssal transport is likely due to some lack of realism in the simulation of abyssal water production due to the simple parameterization of convection at high latitudes and/or unrealistic rates of vertical diffusive exchange of abyssal and surface waters. Either process could lead to an imbalance in the model thermohaline state that might favor an unrealistic transient reorganization of water masses by horizontal advection. After only 10 years of integration, the model is unlikely to be in thermodynamic equilibrium, and from the comparison here we would caution against using the model results to infer general features of the mean oceanic thermohaline circulation that were not supported by observation.

The encouraging comparison of variability suggests the dynamic processes that account for the transient motions in the ocean are simulated well, regardless of whether the model has yet achieved an equilibrium mean circulation. This suggests variability in the DWBC is largely unconnected with processes in the thermohaline source and sink regions. An obvious dynamical explanation for the variability is the presence of planetary waves generated by surface wind and buoyancy flux variations. In the next section, we review properties of planetary waves that we use to build a case for their role in the transport variability.

5. Planetary Wave Theory

The ocean's response to large-scale, low-frequency changes in wind and surface heating is the generation of planetary (Rossby) waves, the theory of which is described by, e.g., *LeBlond and Mysak* [1978, section 18] and *Gill* [1982, section 12]. These are horizontally propagating plane waves with east (x) and north (y) velocity components of the form

$$(u, v) = (U_0, V_0) F_n(z) \exp [i(kx + ly - \omega t)]. \quad (1)$$

In a flat-bottom ocean the horizontal wavenumber components k , l and frequency ω satisfy the dispersion relation

$$\omega = -\beta k / (k^2 + l^2 + 1/R_n^2) \quad (2)$$

where β is the variation of the Coriolis frequency with latitude. The Rossby radius R_n and vertical structure $F_n(z)$ of each mode are determined numerically from an eigenvalue problem that depends on the observed vertical stratification. Mode 0 through 4 solutions are shown inset in Figure 7 for the mean stratification in the PCM-9 region.

The dispersion relation (2) is plotted in Figure 7 for $l = 0$. For each mode, ω is maximized if l is zero, so a continuum of waves is possible between the k axis and the zonal ($l = 0$) dispersion curve. The zonal dispersion curve is thus a limit curve defining the legal frequency range for planetary waves at given k . At any given frequency, and $|l|$, there exist two possible waves. Both have negative (westward) zonal phase velocity, $c = \omega/k$, but the longer and shorter waves have westward and eastward zonal group velocity ($c_{gx} = \partial \omega / \partial k_x$), respectively. As l varies, the boundary between westward and eastward group velocity moves in $k - \omega$ space along the locus identified in Figure 7 as the dotted shortwave/longwave separation curve, $k = -\beta/2\omega$. This curve is the same for all modes. The dispersion limit curves, and the short-wave/long-wave separator curve, will be used below to help interpret space-time spectra.

Long planetary waves propagate westward until they encounter a western boundary, such as the Kermadec Ridge, where they can reflect into short waves with eastward group velocity. The western boundary of an ocean thus acts as a source of short planetary waves [Pedlosky, 1965]. From the slope of the dispersion curves, we see that short waves have substantially slower group speed than long waves. Reflected short waves therefore have higher energy density than incident long waves, in order to conserve energy flux. The ratio of

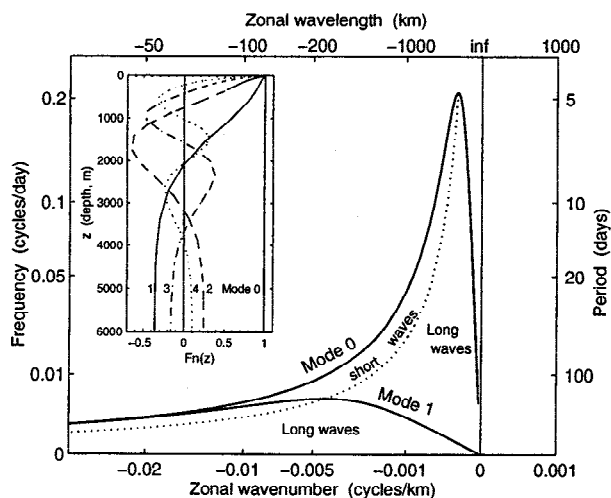


Figure 7. Planetary wave dispersion curves (solid line) for zonal propagation ($l = 0$). These are the upper frequency limits for waves of given mode. The curves for nonzero meridional wavenumber all fall below the respective solid line for each mode. The dotted line is the long-wave/short-wave separator: waves to the left have eastward group velocity, those to the right have westward group velocity. The axes are stretched to improve visibility of the long-wave region. Inset shows vertical mode structures at PCM-9 for modes 0–4. Rossby radii are 1560, 37, 17, 11, 8.7 km for modes 0, 1, 2, 3, 4, and 5, respectively.

kinetic to potential energy is proportional to wavenumber squared [Gill, 1982], so short waves have most of their energy in kinetic form. Both these factors favor the observation in current-meter data of short waves, rather than long waves, because of their higher velocity variance.

A further property of planetary waves is that the particle orbit is strongly polarized perpendicular to the wavenumber vector, so that the velocity components (U_0 , V_0) in (1) are proportional to $(l, -k)$. The north-south scales of wind systems that influence the meridional wavenumber are typically several hundred kilometers [Gill, 1982]. We will see that this scale is bracketed by the zonal wavenumbers we find for typical short and long waves in the data. Therefore we expect meridional and zonal velocity variability to have distinct characters, with meridional variability dominated by short waves which carry energy east, and zonal variability dominated by long waves carrying energy west.

There have been several observations of low-frequency variability consistent with planetary wave theory. In the North Atlantic, McWilliams and Flierl [1976] found the superposition of two barotropic and two baroclinic free planetary waves was sufficient to account for 70% of the observed signal in current-meter data from the Mid-Ocean Dynamics Experiment (MODE). Using the positions of a cluster of SOFAR floats to estimate relative vorticity, Price and Rossby [1982] explained a similar fraction of the observed variability in the POLYMODE Local Dynamics Experiment with a single barotropic wave. Semiannual period baroclinic waves were observed in altimeter data in the South Atlantic by Le Traon and Minster [1993], and the recent analysis of TOPEX/POSEIDON altimeter data by Chelton and Schlax [1996] shows baroclinic waves to be a ubiquitous feature of the World Ocean.

6. Space-Time Variability

If freely propagating planetary waves are present on timescales from a few days to years, they should be apparent as crests and troughs in longitude-time diagrams (referred to as “Hovmueller” diagrams in meteorology). Hovmueller diagrams of the velocity at the nominal 2500-m level of PCM-9 and the closest model level are shown in Plate 1. Both are dominated by westward phase propagation. In the analysis that follows, we show that this is indeed the signature of planetary wave propagation.

The dominant timescales and space scales appear different in model and data. In the model the waves are more persistent, though in PCM-9 there is a persistent train of crests and troughs with about a 150-day period west of 175°W. We will use the terms crests and troughs for positive (red) and negative (blue) anomalies, respectively.

We have already seen that examples of individual velocity records compare poorly, so it is not surprising that the Hovmueller diagrams differ. However, we know transport variabilities in data and model have similar zonal length scales and energy level, and time series of total abyssal transport are significantly coherent at most frequencies. Therefore there must be key processes which are well modeled and which must be present in both model and data in Plate 1, yet are somehow obscured in the Hovmueller diagrams.

6.1. Wave Characteristics in Data and Model

Period and wavelength are difficult to estimate for the propagating features in the PCM-9 Hovmueller diagrams because crest and trough amplitude vary with distance from the Kermadec Ridge and decay or break up around the Louisville Seamounts. However, the train of crests and troughs in PCM-9 west of 175°W is amenable to analysis. The separation of the crests suggests the order of a 150-day period and 200–400 km zonal wavelength. Neither parameter is easy to estimate, but wavelength is the more difficult, since the waves appear to break up only one (e.g., day 450) to two (e.g., day 350) wavelengths from the Kermadec Ridge. The slope of the crests indicates a phase speed of 2.0–2.3 cm s⁻¹, implying 300-km wavelength at 150-day period. These parameters are consistent with barotropic, or possibly near-maximum frequency baroclinic, free planetary waves, falling along the short-wave/long-wave delimiting curve (Figure 7). The source of this energy may be an instability in the DWBC, or planetary long waves at the same period carrying energy westward from the Pacific. We return to this point below but note the presence in PCM-9 data in Plate 1 of near-vertical streaks at a variety of timescales that may be waves of length very much longer than the array, with fast phase speeds and westward energy flux. The PCM-9 zonal velocity shows evidence of the first few crests and troughs of the order of a 150-day wave, though these are less clear than in the meridional velocity. The near-vertical streaking is perhaps slightly more evident than in the meridional velocity.

Model meridional velocity at 2475 m is dominated by an approximately 50-day wave of 400- to 500-km wavelength and zonal phase speed about 10 cm s⁻¹. This wave is much clearer than the 150-day wave in PCM-9, though it does display a similar disruption of crests at the Louisville Seamounts and tendency for marked reduction of phase speed near the Kermadec Ridge. This wave falls in the short planetary wave regime and consequently carries energy eastward from the ridge.

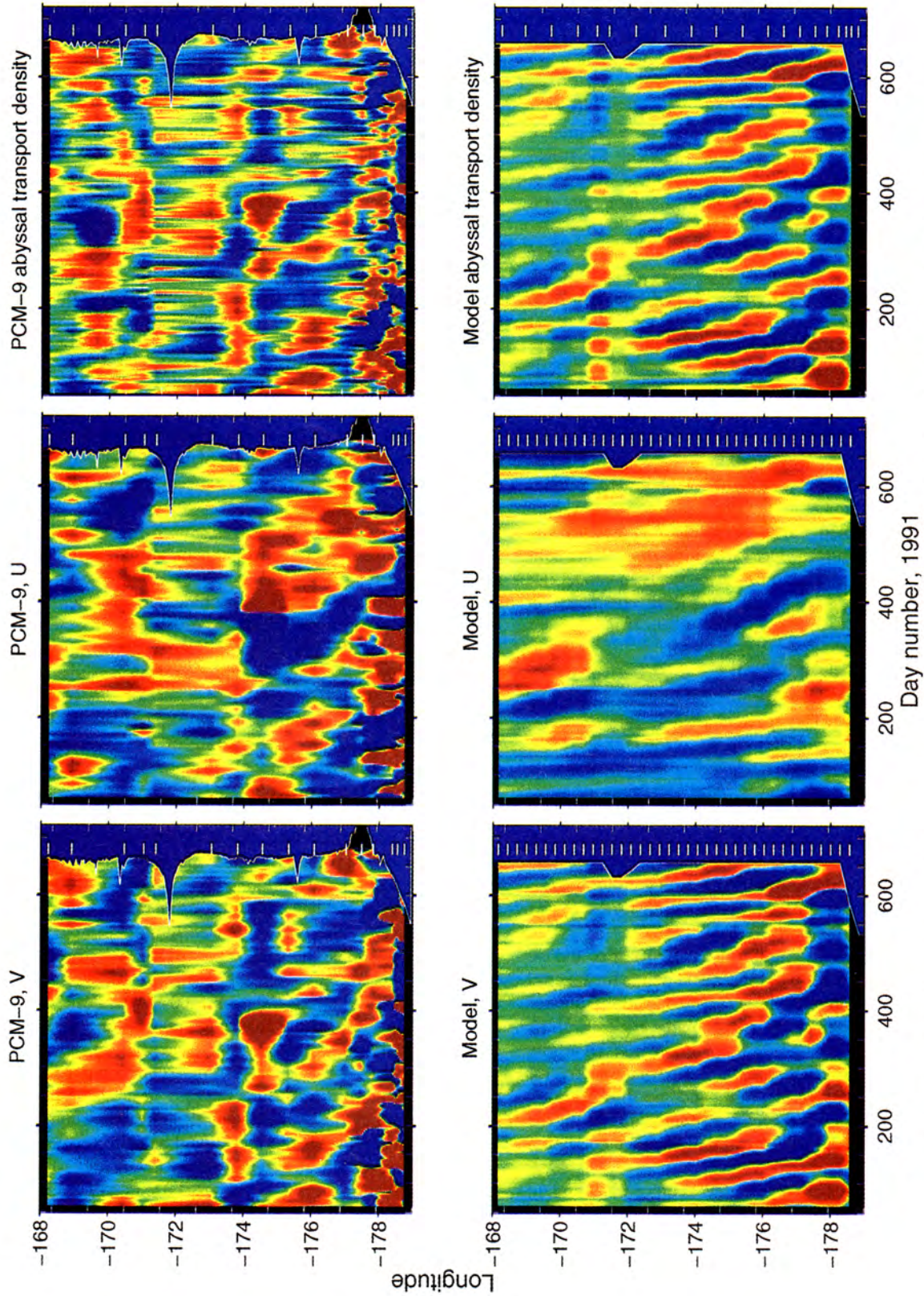


Plate 1. Hovmöller (longitude-time) diagrams of the velocity at 2500 m for PCM-9 (top) and model (bottom) with bathymetry overlaid at right. (left) Meridional velocity v , (center) zonal velocity u , (right) depth-integrated meridional velocity or "transport-density" in Sv km^{-1} . In these and all following Hovmöller diagrams the time mean is removed at each longitude, and the scale is +3 (red) to -3 (blue) cm s^{-1} . (Greater magnitudes take the extreme color value.)

The right-hand panels of Plate 1 show depth-integrated meridional velocity. This is effectively transport density (with units of Sv km^{-1}) and, when integrated with respect to longitude, gives the total abyssal transport time series (Figure 6). Variability in this quantity is more directly related to transport variability than are the series from individual levels. For both model and data, the dominant waves seen in the 2500-m velocity are still present but are deemphasized. This results from vertical shear causing slight misalignment of crests at different depths. Although the 150-day wave is not evident in the model, we know there is considerable coherence between the transport time series at this period. Conversely, the 50-day wave, dominant in the model yet not apparent in the data, falls at a period of poor coherence between transport time series.

In Hovmueller diagrams for both model and data, waves consistent with planetary short, or zonally static, waves are the eye-catching features. There are some signs of rapidly propagating long waves in the form of near-vertical streaks: most evident in the vertically integrated abyssal transport density. As noted in the discussion of planetary wave theory, the emphasis on short waves, rather than long waves, is expected in velocity data. We argue below that the processes which are coherent between model and data are principally long waves which force the short waves seen above by reflection at the western boundary, but which are themselves not highly visible in Hovmueller diagrams.

It is the short reflected waves in Plate 1 that obscure the underlying coherence in transport variability. Integrating zonally to form the net transport time series tends to cancel out the short wavelengths, so that the significant coherence in Figure 6 can appear.

6.2. Wavenumber-Frequency Spectra

We can improve on the wave parameters estimated above by wavenumber-frequency (k - ω) spectral analysis and, more important, detect weaker waves that are not obvious in the Hovmueller diagrams. This analysis models data as a linear superposition of sinusoidal plane waves. Any variability of wave properties in space or time results in estimation of broad peaks, with preference in fitted energy level given to waves which are the most persistent and invariant. Spectra are computed in the conventional manner by smoothing periodograms calculated from two-dimensional Fourier transforms of the data [Priestley, 1981, equation (9.7.17)].

The model results are on a uniform (26.4 km) grid, and we interpolate the PCM-9 data to the same grid points for spectral analysis. Interpolating an irregularly sampled spatial sequence prior to computing spectra can cause problems, typically in the smearing or loss of spectral peaks [e.g., Moore and Thomson, 1991]. However, we experimented by comparing spectra for the two model data sets (grid point, and mooring location interpolated to grid point) and found only small effects for the waves of interest, i.e., those with wavelengths large compared to the grid spacing.

The k - ω periodograms are distributed as quasi-independent chi-square-2 variables [Brillinger, 1974, p. 1635] and when smoothed with a nine-point window which is the normalized product of coefficients [$1/2, 1, 1/2$] in each direction they yield spectral estimates with 15 degrees of freedom by the analysis applied by Koopmans [1974, pp. 281–282, equation (8.39)] to multivariate spectra, which have the same generalized Complex Wishart distribution discussed by Brillinger [1974] and which reduce to chi-square in the univariate case. Lower and

upper 90% confidence intervals based on chi-square-15 are factors 0.6 below and 2.0 greater than the spectral estimate [e.g., Koopmans, 1974, p. 274]. In order to express significance on a contour plot, we choose contour intervals at factors of approximately 2 ($10^{1/3}$ was used). If a closed contour is drawn, then the spectral level within that contour is at least a factor of 2 different from that outside and is therefore significantly different at the 90% level. Negative frequency quadrants are redundant and are not plotted.

Figure 8 shows spectra for each of the panels of Plate 1. Bandwidths, indicated by the small boxes in each plot, are large compared with the scales we would like to resolve, and at periods less than about 30 days, they smear across the entire planetary wave dispersion region. However, we cannot reduce bandwidth without reducing smoothing, which is already minimal.

The spectra show energy clusters within and around the legal dispersion region for planetary waves, and the largest spectral peaks lie within it. Integrals show approximately 35% of velocity variance lies within the planetary wave dispersion region for the PCM-9 data, and 60% for the model. There are several possible reasons for this. High wavenumbers are not resolved in the meteorological analyses used to drive the model, so energy at these scales will not arise directly from surface forcing. While the model resolution is high by global model standards, 26.4 km is still marginal for representing nonlinear instability or wave interaction processes that would generate higher frequency variability. Waves with dispersion properties outside the planetary wave regime include topographic waves, for which the restoring force is the vortex stretching of the bathymetric slope. In level coordinate models such as the LANL model, where bathymetry is discretized in a series of steps, this vortex stretching is approximated poorly, and the dispersion properties of topographic Rossby waves may not be simulated well (D. B. Haidvogel and A. Beckmann, Numerical models of the coastal ocean, submitted to *The Sea*, 1997). We will show below that underestimation of the order of 50-day topographic waves by the model is responsible for the breakdown of abyssal transport coherence at that period.

The largest spectral peaks lie within the planetary wave region and correspond with the most obvious waves in the Hovmueller diagrams. The PCM-9 meridional velocity spectrum peaks at 200-day period, 250-km wavelength, but the peak includes the 150-day, 300-km coordinates estimated from Plate 1. However, the process is clearly not a simple monochromatic wave, since the peak is part of a general broadband continuum of elevated energy between about 100 days and the record length and about 100 and 1000 km in both velocity component spectra. Within this range there is energy at periods that, according to planetary wave theory, can only be for barotropic waves, but also at periods that could be either barotropic or mode-1 baroclinic waves.

There is energy on both sides of the short-wave/long-wave separator curve, though the meridional velocity spectrum favors shorter waves and the zonal velocity favors long waves, as anticipated. Wavelengths greater than the length of the PCM-9 array are registered along the zero-wavenumber axis. The separation of scale by velocity component is more evident in the model spectra. The presence of both long and short waves suggests reflecting pairs may exist, and there are some signs in the spectra that this is so. Note, for example, the alignment of broad longwave peaks in u with shortwave peaks in v at very long periods in PCM-9 and at 50 days in the model.

There are notable similarities in model and PCM-9 spectra.

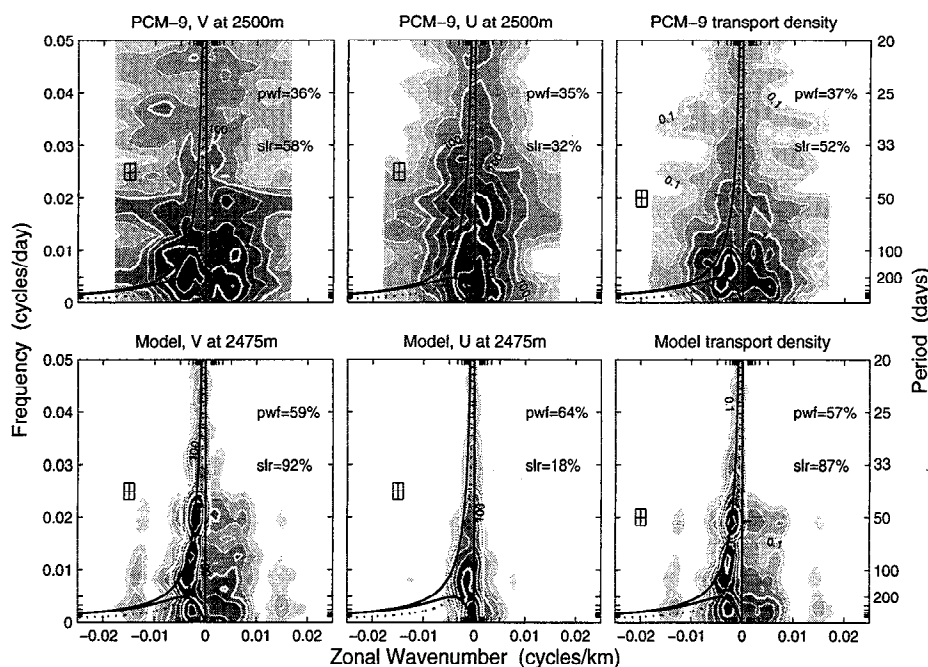


Figure 8. Frequency-wavenumber spectra for the data sets of Plate 1. The unlabeled ticks are at periods 300, 400, ..., 1000 days and at wavelengths 200, 300, ..., 1000 km. Tabulated on each plot is the fraction of energy lying within the planetary wave zone “pwl” and the ratio of short to long planetary wave variance “slr.”

Model and data zonal spectra show two major peaks at around 50 days and from 80 days to record length, both confined largely to the planetary long-wave region, though the data show more energy spilling over to positive wavenumbers. In both cases, there is a distinct dip at 60–70 days. Meridional spectra have greater differences. At semiannual scales corresponding to the dominant waves in the PCM-9 Hovmueller diagram, the model underestimates the spectral level, whereas at annual scales it is very slightly overestimated. The model has a broad peak (the largest) at around 50 days, but in PCM-9, energy splits into a small peak at just less than 50 days and a wide ridge of energy at periods just greater than 50 days, with a peak at positive wavenumbers. The positive wavenumber ridge also occurs in the model and peaks at about 500 km (positive) wavelength, but with a decade less energy. It seems similar processes are present, but the model overestimates the planetary short wave at the expense of the positive wavenumbers.

The same is found in the transport density spectra. The peak splitting at 50 days is reduced in PCM-9, and a broad peak in the planetary wave region dominates, as in the model, though the model has relatively more energy in the short waves. We associate this preference for short waves with the anomalously strong 50-day wave in the model Hovmueller diagram. Model and data both show ridges of energy at positive wavenumbers at 50 days and also at longer periods. In all cases, positive wavenumber energy is underestimated by the model.

6.3. Separating the 50-Day Wave

The 50-day period is of special interest because at this period the model and observed abyssal transport have the lowest coherence. Band-pass filtering (25–75 days) isolates an order 50-day wave in the model velocity (Plate 2). The meridional component has the greater amplitude, and this decays eastward toward the Louisville Seamounts where most wave crests appear to undergo a change of slope. West of the seamounts,

phase speeds are about 10 cm s^{-1} , in agreement with the 50-day, approximately 500-km short-wave peak in the spectrum. The zonal component shows evidence of a much faster, much longer, wave of this period east of the seamounts. The slope is too steep to estimate, and the wavelength is clearly much longer than 1000 km. The black tick marks in the right-hand panels of Plate 2 are at the same 50-day intervals and are provided to highlight these waves and indicate the correspondence of modeled and observed crests. These waves are presumably responsible for the very long wavelength peaks in both model and PCM-9 zonal spectra (Figure 8). This wave seems to be a key link between the model and data. The lack of coherence in the transport at 50 days must be due to differences in the way the 50-day long wave interacts with the Kermadec Ridge in model and data.

In the model the long waves reflect as planetary short waves that decay with the 600–800 km overall scale of the DWBC, implying a frictional spindown time of the order of 100 days. This wave is only weakly apparent in the observed spectra. More obvious in the band-passed PCM-9 Hovmueller (Plate 2) is a wave confined to the flank of the Kermadec Ridge with eastward phase velocity (positive slope to crests). This cannot be a planetary wave; it must be a topographic wave. *Pickart and Watts* [1990] found 40-day bottom-trapped topographic waves account for significant variability in the DWBC of the mid-Atlantic shelf. Their evidence was a comparison of features of the 40-day signal with topographic wave theory.

Cross spectra of velocity for the 2500-m current meters at moorings 1 and 2 (Figure 9) show a significant peak in coherence that includes the 50-day period, and the phase lag implies downslope propagation at about 5 cm s^{-1} as expected of topographic waves. This is evidence that the 50-day, 200-km (4.6 cm s^{-1}) peak in the $k - \omega$ spectra comes from variability on the ridge.

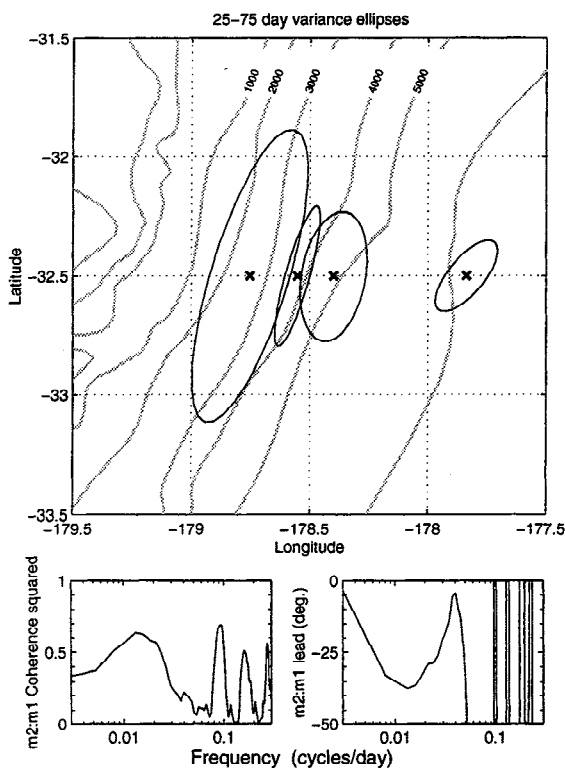


Figure 9. (top) Velocity variance ellipses for 25- to 75-day band for the deepest current meters on the Kermadec Ridge. (bottom) Coherence and phase of 2500-m instruments at moorings 1 and 2.

For the 200-km wavelength observed, and a buoyancy frequency of the order of $N = 10^{-3} \text{ s}^{-1}$ at 4000-m depth, there is strong bottom trapping [Pedlosky, 1965] and the dispersion relation for topographic waves is approximately $\omega = N\alpha \sin \theta$, where α is the bottom slope and θ the angle the wavenumber makes with the downslope direction [Pickart and Watts, 1990]. On the Kermadec Ridge $\alpha \approx 0.06$, and a 50-day wave should propagate at only $\theta = 1.4^\circ$ anticlockwise from downslope. The wavenumber is orthogonal to the major axis of velocity variability, so velocity variance ellipses should be oriented about 1.4° anticlockwise from isobaths. Figure 9 shows variance ellipses computed from the 25- to 75-day band-passed velocity at the bottom current meters on the ridge. The orientation is very close to along isobath in all cases, with a tendency to favor the expected weak anticlockwise rotation.

These estimates of topographic wave parameters are only approximate; we make no attempt to remove variability due to 50-day planetary waves that may interfere with estimating the topographic wave phase speed, and we are uncertain what effect variations in isobath direction near the moorings might have on the orientation of the ellipses. The key point, however, is that data from the bottom current meters are consistent with features of topographic wave dispersion.

Thus in the observations the energy of the 50-day long-waves is lost within a boundary zone of about 100 km, consistent with the scale set by topographic waves, whereas in the model this energy is dissipated over a 600-km scale set by short planetary waves. We speculate the topographic wave is ill-modeled due to the staircase discretization of the bathymetry simulating poorly the vortex stretching that maintains the waves and/or the excessive dissipation in the model boundary layer that was

revealed in the comparison of modeled and observed mean velocity and eddy kinetic energy.

Wind anomalies in the 30- to 70-day band, associated with the atmospheric Madden-Julian Oscillation, have been shown by Kiladis *et al.* [1994] to have a strong curl at 30°S over the Southwest Pacific Basin. It is therefore not unexpected to see energy at this period in the planetary wave field.

7. The Larger Model Domain: Basinwide and Decadal Scales

We now examine variability in the model beyond the sampling limits of PCM-9. We extend the spatial domain to the full Pacific transect at 32.5°S and extend the time domain 2 years beyond the PCM-9 deployment period. We do not consider years prior to 1991 because mode 1 baroclinic waves take of the order of 6 years to propagate from the East Pacific Rise to the Kermadec Ridge, and until this time passes, variability due to remotely forced planetary waves may not be simulated well.

7.1. Zonal Variations

Hovmueller diagrams for model velocity at two depths are shown in Plate 3. We consider the 2475-m depth first. Discussion of the Tasman Sea (west of 180°), which is largely shallower than this depth, is deferred until after velocities from the deeper level are presented.

The most energetic feature of the meridional component is the eastward decaying 50-day waves seen previously in the PCM-9 region. These were shown to be planetary short waves, and we argued that they were forced by the reflection of long waves whose zonal scale was much greater than can be resolved in the PCM-9 region. Here we see that similar bands of 50-day waves occur at the East Pacific Rise (110°W) and to a lesser extent at the Chile Rise (90°W). The PCM-9 observations showed wave energy is greatest adjacent to the Kermadec Ridge and that some of the long-wave energy is lost to topographic waves, but this energy transfer is underestimated in the model. It is likely then that the model also underestimates topographic waves at the East Pacific Rise.

The expanded spatial domain shows more clearly than previously what appear to be the long waves responsible for generating the short waves. There are intense steep crests with 30- to 50-day separation in zonal velocity east of the Louisville Seamounts from 170° to 145°W . These wax and wane in intensity. Although they have very long wavelengths, they do not appear to occupy the whole basin.

To examine zonal variation of the wave field, we compare $k - \omega$ spectra for the 2475-m velocity in subregions: the western half of the Southwest Pacific Basin (WWP) from 180° to 150°W , and the eastern half of the Southwest Pacific Basin (EWP) from 150° to 120°W (Figure 10). For clarity, the spectra are contoured at 1/2 decade, as opposed to 1/3 decade used in Figure 8.

Zonal long-wave energy rises by an order of magnitude from EWP to WWP, indicating long waves are enhanced in the western half of the basin. We speculate that this may be a consequence of the waves being exposed to continuing forcing, with a consequent increase in amplitude, as they propagate westward. The corresponding westward increase in short-wave energy, particularly at periods less than 100 days, is consistent with the notion that short-wave energy is locally generated by long-wave reflection or scattering; in the west there is more incident long-wave energy available. Within the EWP region

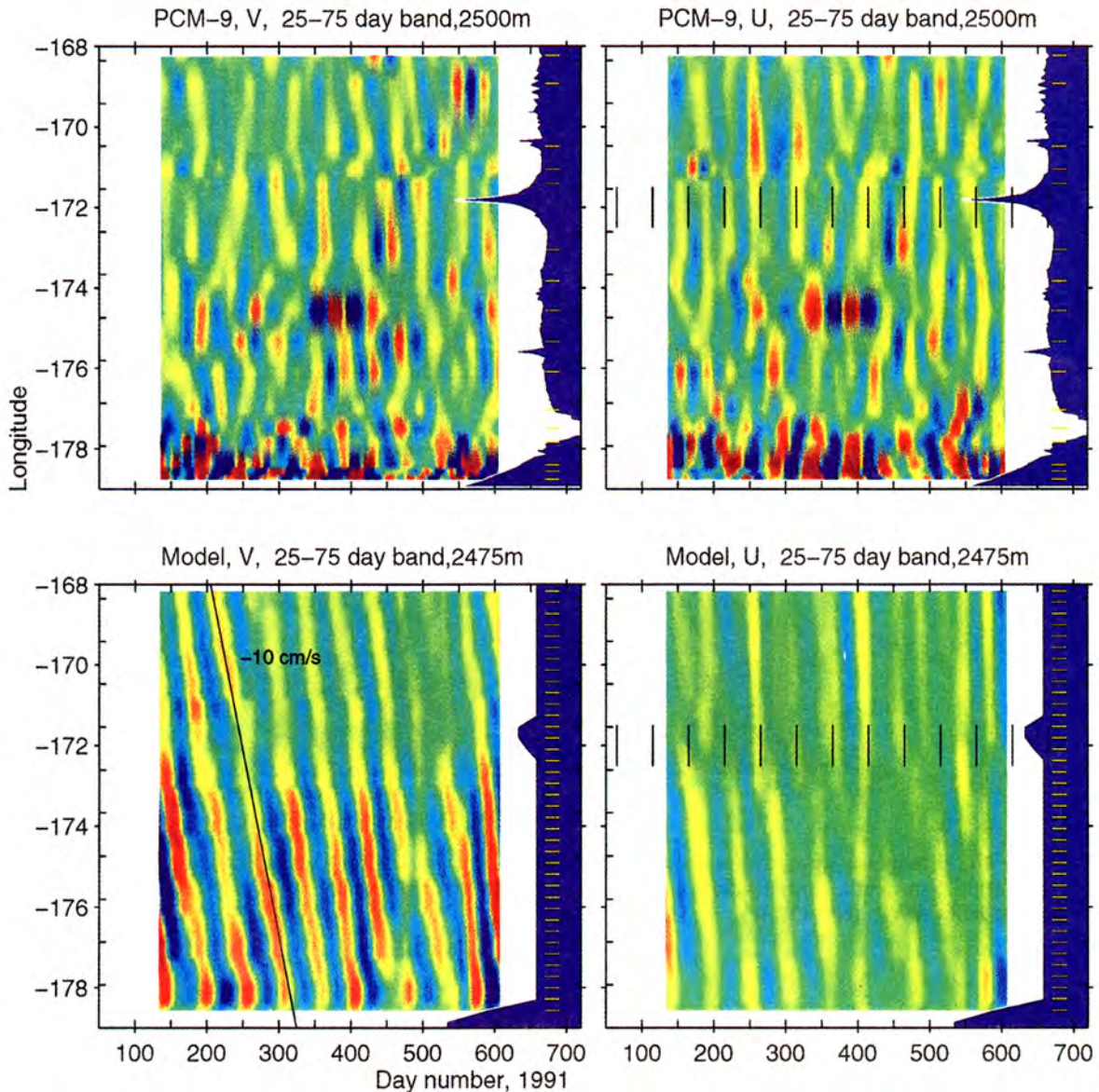


Plate 2. Bandpass filtered (25–75 day) velocity at 2500 m (compare to Plate 1) for PCM-9 (top) and model (bottom). (left) Meridional velocity v , (right) zonal velocity u . Vertical tick marks in right panels at 50-day intervals indicate coherent long waves in model and data. Horizontal tick marks on bathymetry show location of current meters or grid points.

the high-frequency meridional component energy is not appreciably different either side of the long-wave/short-wave separator, consistent with there being no significant bathymetric features to generate short waves.

In the Hovmueller diagram for the 117-m meridional velocity (Plate 3) at about 130° to 140°W there are slow waves of roughly semiannual period, with zonal wavelength of 400–600 km. These also show faintly in the 2475-m zonal velocity. These parameters lie in the planetary long-wave dispersion regime, and we associate these waves with the semiannual long waves we postulated to be the source of the dominant short waves in the PCM-9 array, and which correlated model and PCM-9 deep transport time series at this timescale. These waves are also apparent in the appropriate spectra: as a broad peak in the EWP u spectrum of Figure 10 and as a sharper peak, just above the mode-1 curve in the EWP v spectrum for 117 m in Figure 11.

7.2. Vertical Variations

Comparing Hovmueller diagrams for 117 and 2475 m (Plate 3) shows velocity variance is greater at shallow than at abyssal levels. We do not show all levels because of consideration of space, but note that the 117-m results are typical of the shallow levels, and 2475 m is typical of the deeper levels. The change in character occurs at around 1000 m, which coincides with the crest of the Kermadec Ridge.

The deep and shallow $k-\omega$ spectra (Figures 10 and 11) show different emphases on different waves. In the WWP region, short-wave energy at periods less than 100 days is only around 1/2 decade more energetic at 117 m than at 2475 m, but at annual and longer periods, long-wave energy at 117 m is 1–1.5 decades greater than at 2475 m and, at semiannual periods, more than 1.5 decades greater. In the EWP region the

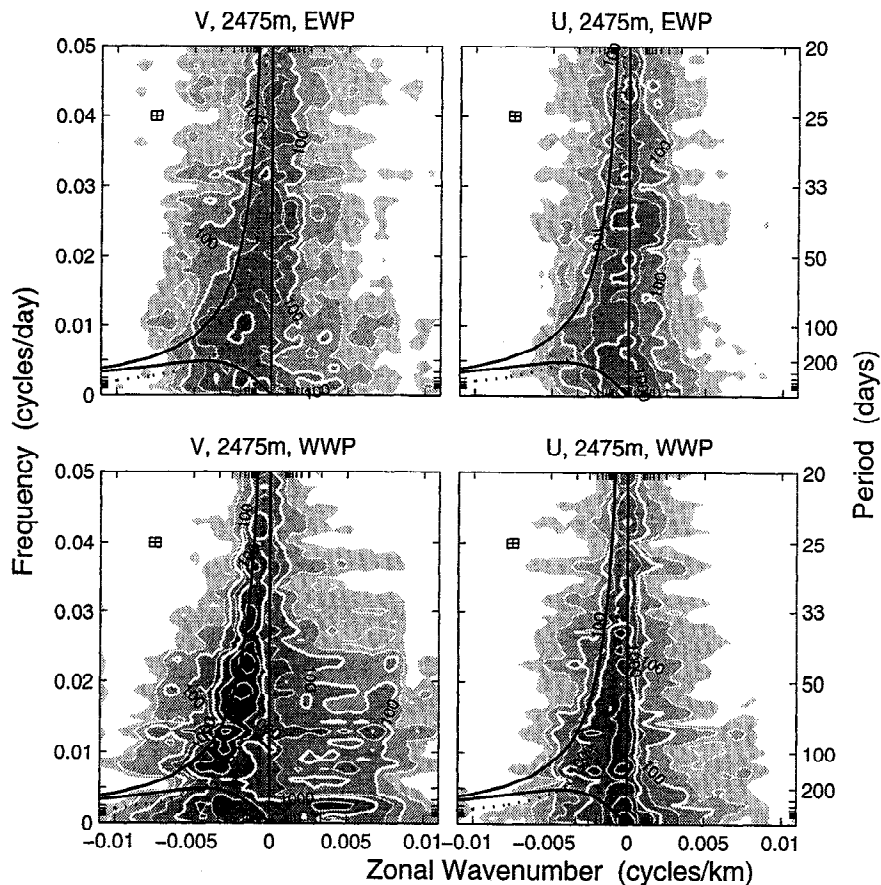


Figure 10. Frequency-wavenumber spectra for model meridional (left) and zonal (right) velocity components at 2475-m depth. (top) Eastern half of the Southwest Pacific Basin (EWP: 150°–120°W); (bottom) western half (WWP: 180°–150°W).

major difference is that semiannual period long-wave energy is a decade more energetic at 117 m than 2475 m.

Higher energy at shallow depths occurring at semiannual and longer periods suggests the presence of low-mode free baroclinic waves. We explore these spectral differences further by decomposing the vertical structure.

7.3. Separating Barotropic and Baroclinic Motions

The PCM-9 current meters were deployed below 2500 m only, making it impossible to separate baroclinic and barotropic motion. There is no such limitation on the model output. Here we estimate the barotropic component as simply the depth average velocity, and the baroclinic component as the residual of velocity from its depth average. (This may not work well over the shallow Tasman Sea, where the average is constructed over a depth interval above the zero crossing in mode 1).

Plate 4 shows the barotropic velocity and the derived baroclinic anomaly velocity at 2475 m. We have not shown the baroclinic field at 117 m for reasons of space, but note that it is very similar in appearance to that at 2475 m, except for being slightly more energetic and a mirror image, in the sense that troughs match to crests of the deeper level. This is expected if low-mode baroclinic motions dominate. The two-dimensional (2-D) correlation coefficients are high at -0.93 between zonal baroclinic velocity at 117 m and 2475 m, and -0.87 between the meridional baroclinic velocity. Conversely, the zonal to meridional component correlations are low at -0.07 , -0.04 ,

-0.16 for the barotropic and the 2475-m and 117-m baroclinic variability, respectively. This is expected, given that the two components favor uncorrelated short and long waves with opposite group velocity.

The similarity of the barotropic velocity to the unseparated 2475-m velocity (Plate 3) argues that most of the variability at this depth is barotropic, at least at high frequency. The baroclinic velocity is dominated by waves with semiannual to annual periods and 600- to 800-km wavelength. In earlier discussion of the unseparated meridional velocity, we noted the semiannual crests in the 130°–140°W region and suggested they were long waves responsible for generating the short semiannual waves corresponding to the dominant peak in the PCM-9 meridional spectrum. This plate confirms these waves are dominantly baroclinic.

At semiannual to annual periods the baroclinic meridional spectra in the WWP region are similar in form at different depths, except that the 2475-m depth (Figure 12) has slightly higher energy levels than are found at 117 m (not shown). In both cases the meridional spectra for the WWP region have distinct ridges of long-wave energy lying along the frequency limit curve for mode 1 baroclinic waves.

If the baroclinic components were uncorrelated with the barotropic field, the sum of the baroclinic spectrum at a given level and the barotropic spectrum would yield the full-component spectrum at that level; variance of independent variables is the sum of the individual variances. Consequently,

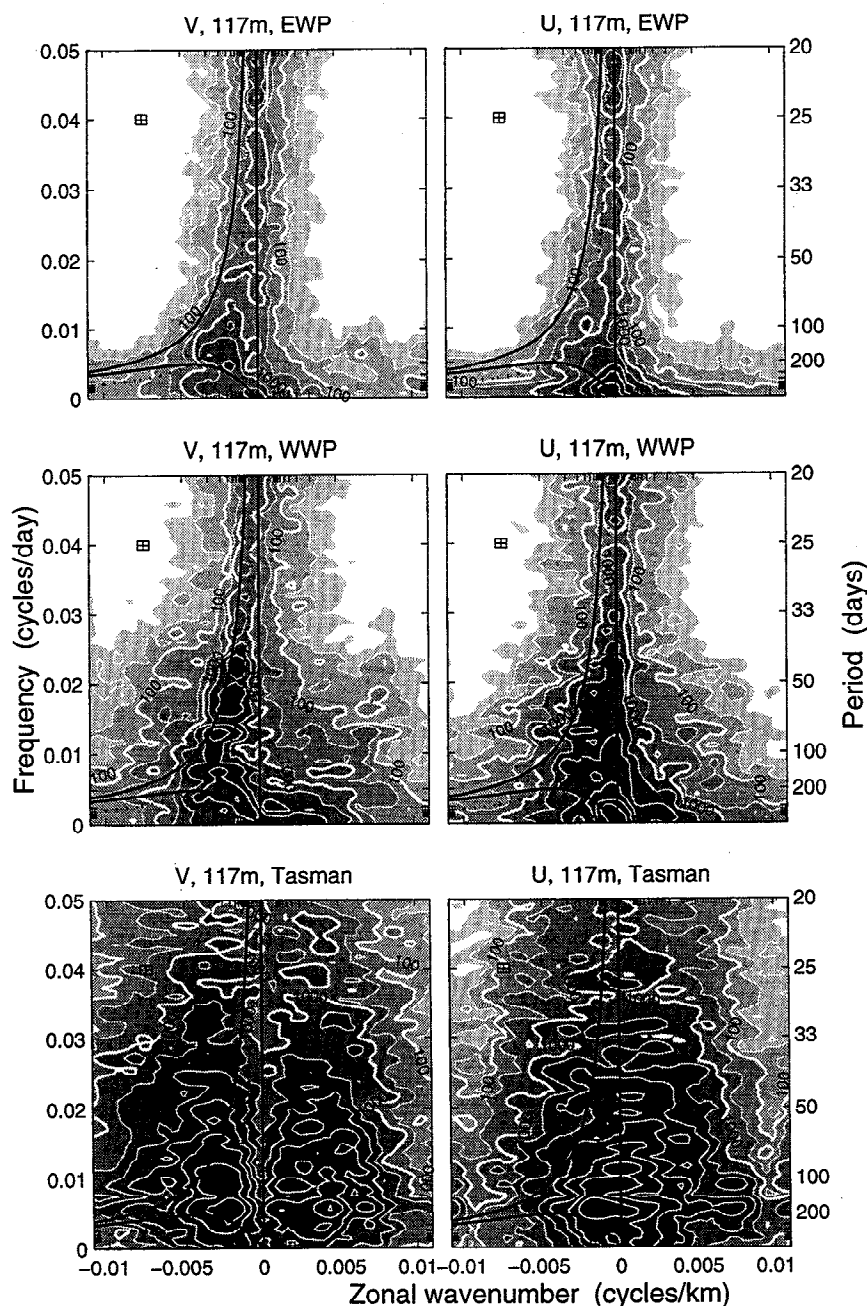


Figure 11. Frequency-wavenumber spectra for model meridional (left) and zonal (right) velocity at 117 m. (top to bottom) Eastern (EWP) and western (WWP) halves of the Southwest Pacific Basin and Tasman Sea (150°E–180°).

the barotropic spectrum would be less energetic than the unseparated component spectra at any level.

What we see in the semiannual to annual period range in the WWP region is that the barotropic meridional spectrum (Figure 13) has less energy than the unseparated meridional component at 117 m (Figure 11) but more than the corresponding 2475-m flow (Figure 10). That the shallower unseparated spectrum is enhanced relative to the barotropic, while the lower is reduced, is evidence that the baroclinic velocity correlates with the barotropic and that it acts to diminish flows at depth while enhancing them near the surface. These features of the spectra are further evidence of planetary wave reflection. At a submerged ridge the boundary condition of zero flow normal to

the bathymetry will be met by the presence of several modes of the same frequency interfering destructively at depth and constructively near the surface. A similar analysis works for the WWP zonal component spectra, and also for the EWP region, but the near-surface enhancement is less marked there.

7.4. Tasman Sea

A large body of observations exists in the Tasman Sea and East Australian Current, and a detailed investigation of the fidelity of the model in this region is beyond the scope of this paper. We simply note here that the character of the velocity variability changes markedly west of the Kermadec Ridge. Spectra (Figure 11) show a major increase in long-wave energy

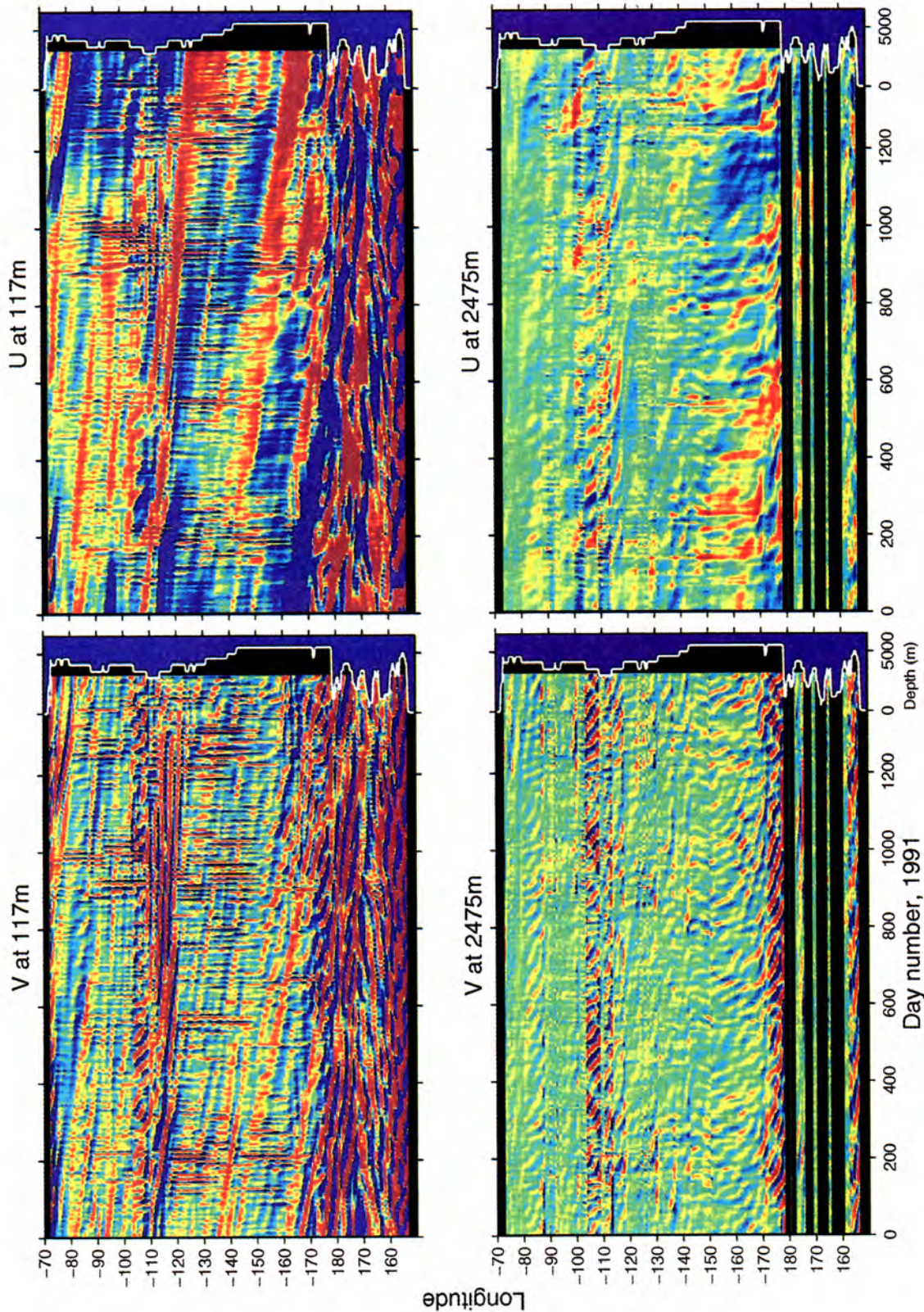


Plate 3. Model velocity for the entire Pacific at 32.5°S at depths 117 m (top) and 2475 m (bottom). (left) Meridional component v , (right) zonal component u , with model bathymetry overlaid at right.

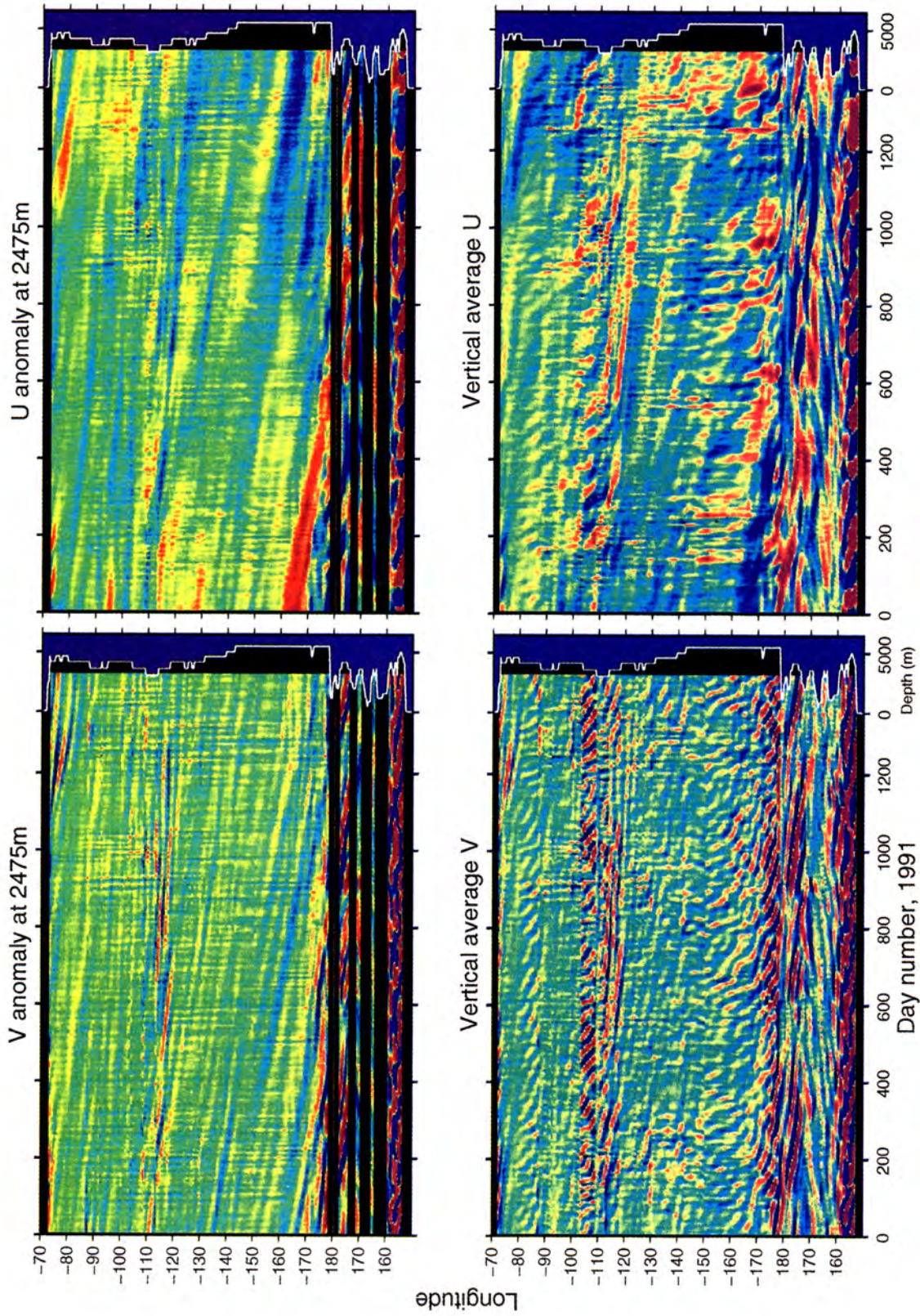


Plate 4. Model 2475-m baroclinic velocity (top) and barotropic velocity (bottom). (left) Meridional component and (right) zonal component.

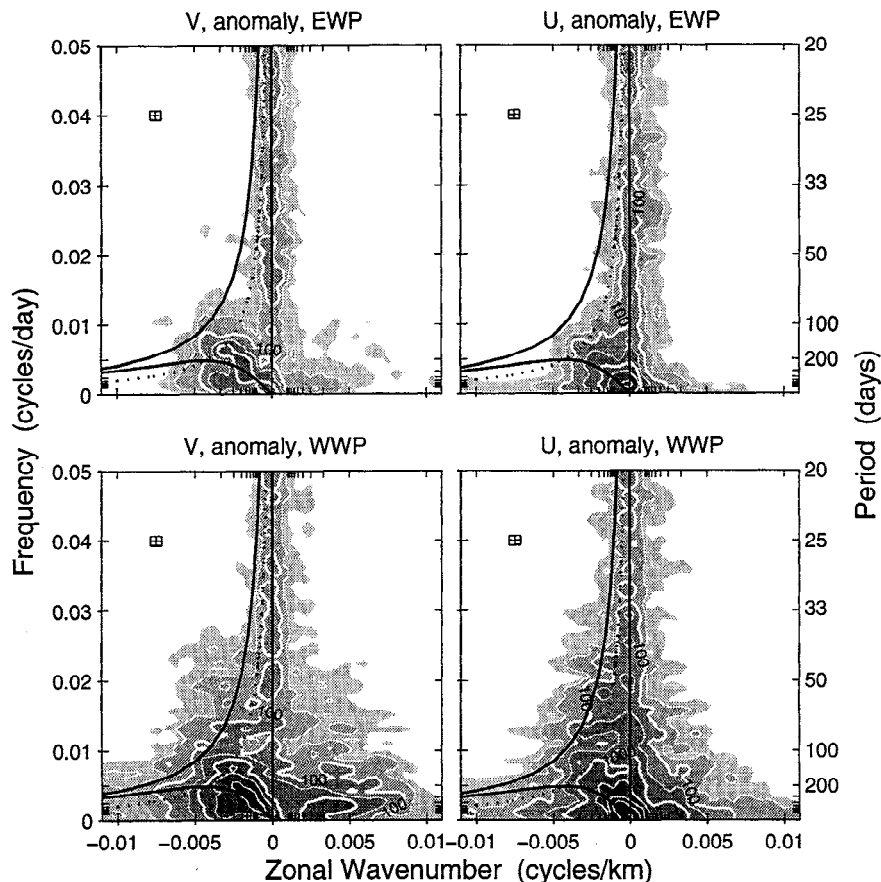


Figure 12. Frequency-wavenumber spectra for model meridional (left) and zonal (right) baroclinic velocity at 2475 m. WWP and EWP regions as for Figure 10.

at semiannual timescales compared to WWP, and this is also apparent in the Hovmueller diagrams (Plate 3). These waves occur in two distinct groups, one on the western flank of the Kermadec Ridge, the other, more coherent and regular, along the Australian shelf. The physical separation suggests dynamic separation. The scattering of planetary waves as they pass over a mid-ocean ridge is known to make the ridge appear as a source of baroclinic waves [Barnier, 1988], but at the Australian coast the variability in the East Australian Current may be of a different character. The irregular bathymetry of the Tasman Sea is likely to further refract planetary waves, and we will not attempt to take the analysis further here.

In the 117-m velocity (Plate 3) and depth average velocity (Plate 4) there is also a sense of slow eastward propagation in the central Tasman Sea. This could be due to topographic waves on the Lord Howe Rise, or eastward propagation of meanders in the Tasman Front.

8. Conclusions

We find the model simulates poorly the mean transport of abyssal waters. We estimate the PCM-9 array shows a 22-month mean northward transport of 20.4 Sv below 2000 m and 17.5 Sv below 3000 m. These estimates are made without recourse to CTD data to define the waters of the DWBC and use elementary interpolation to fill the gaps from failed current meters. An analysis of PCM-9 directed primarily at estimating the mean transport obtained a lower value of 13.6 Sv of northward flow below 2000 m (T. Whitworth et al., submitted paper,

1997). The definition of the DWBC we use is adequate for the goals of this paper: to assess variability and to compare observations with the LANL model. The discrepancy in mean transport between model and data does not require sophisticated analysis to expose: the model 22-month mean northward transport below 2000 m is very low at 0.6 Sv. This is due to a strong, southward, intermediate-depth flow along the Kermadec Ridge and weak model velocity immediately adjacent to the ridge. Integrating below 3000 m excludes much of the southward flow, and the mean transport rises to 3.35 Sv northward, but this is still low compared with any estimate from PCM-9. Model abyssal transport may be low because of poor simulation of abyssal production or vertical diffusive exchange of abyssal and surface waters. In any case, after only 10 years of integration, the model is unlikely to be in thermodynamic equilibrium. From the comparison here, we caution against using the model to infer features of the mean thermohaline circulation not supported by observation.

Time series of integrated abyssal transport in PCM-9 and the model show little spectral dependence on the choice of upper cutoff depth, so assessment of variability is insensitive to this choice.

The PCM-9 observations show two zonal scales in the DWBC mean and variability. Approximately half the mean transport is in a 100-km-wide core confined to the slope of the Kermadec Ridge, with a small recirculation over the adjacent trench. Peak eddy kinetic energy occurs in the same region. A second scale of 600–800 km is evident over which there is a

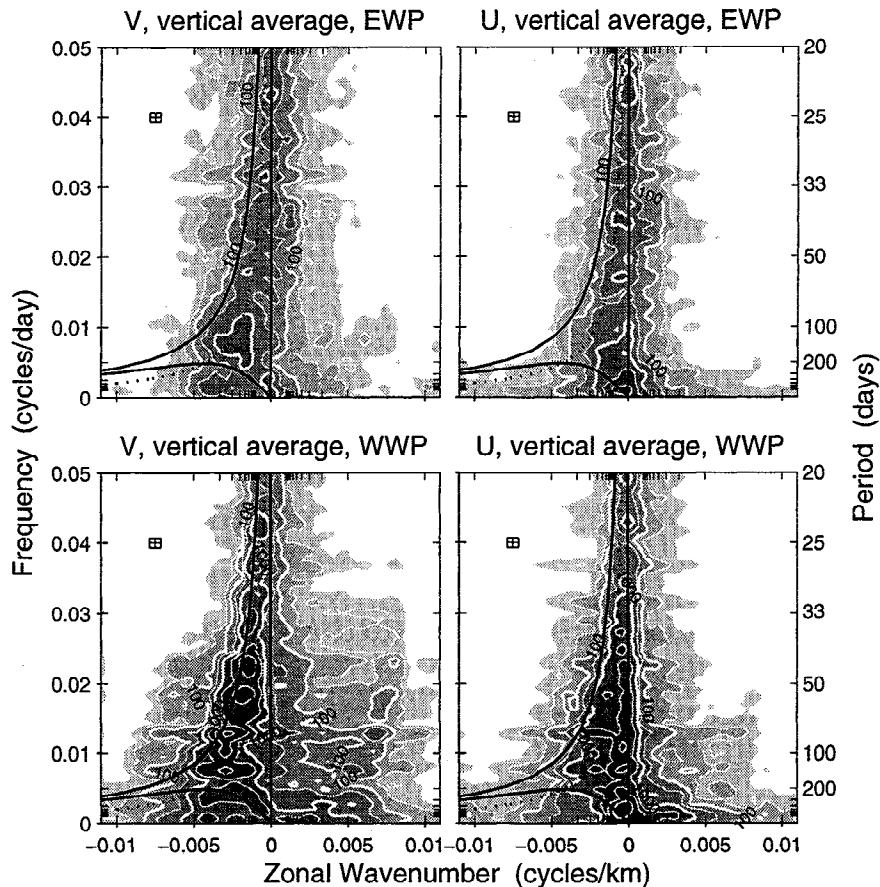


Figure 13. Frequency-wavenumber spectra for model meridional (left) and zonal (right) depth average velocity. WWP and EWP regions as for Figure 10.

further accumulation of mean northward flow and a smooth decay of eddy kinetic energy. Both scales appear in the hydrographic observations of Warren [1970]. The 100-km scale does not appear in the model. The majority of model mean transport occurs in a core of about twice this width, with the maximum velocity mean and variability occurring some 100 km east of the ridge. These features indicate the model has a strongly frictionally damped boundary layer adjacent to the Kermadec Ridge. The eddy kinetic energy is considerably underestimated in this region. The 600- to 800-km scale is not evident in the model mean flow but does appear in the overall eastward decay of eddy kinetic energy, which seems in reasonable agreement with the PCM-9 observations on this larger scale. We associate this scale in the model with the dissipation of short planetary waves generated at the Kermadec Ridge.

Individual current meter time series compare poorly between model and data, but time series of total abyssal transport compare well. Model transport below 2000 m has a standard deviation 8.2 Sv, compared with 13.6 Sv for PCM-9. Both values reduce if 3000 m is used as the upper limit of the DWBC, but the spectral character of the transport time series does not change, and model and data show significant coherence over all timescales except 18–20 and 33–50 days.

The encouraging comparison of transport variability shows the dynamic processes that account for the transient motions in the ocean are simulated well, regardless of whether the model has yet achieved an equilibrium mean circulation. This suggests variability in the DWBC is largely unconnected with

processes in the thermohaline source and sink regions. Moreover, it provides an opportunity to learn more about the variability in PCM-9 by combining model and observations than we could learn from PCM-9 alone. Planetary waves are an obvious hypothesis to explain the variability, and the spacescales and timescales may be much longer than are observable in the PCM-9 data.

We find the following evidence that planetary waves are important in the variability observed by PCM-9: (1) the variability shows distinct domination by westward propagating, wave-like features; (2) in wavenumber-frequency space the energy clusters within and around the legal dispersion region for planetary waves and the peak energy at any period lies generally within this region; and (3) as expected from the theoretical polarization of planetary wave particle orbits, zonal velocity favors long-wave energy and meridional velocity favors short-wave energy.

These things alone do not prove conclusively that planetary wave dynamics explain the observed waves; we require meridional wavenumbers to do that definitively. Nevertheless, these are key signatures, and it is clear that planetary waves define the nature, if not all the detail, of much of the variability.

Outside the planetary wave zone in k - ω space there are peaks that align with peaks at the same frequencies inside the planetary wave zone but with lower energy. We interpret this as variability forced by energy lost from the planetary wave field, and indeed, we have direct evidence of this happening along the Kermadec Ridge in what appears to be a topographic

wave at 50-day period. The fact that the model has a smaller proportion of energy in the nonplanetary wave region is consistent with the model having less bathymetric structure, more friction, and a tendency to simulate topographic waves poorly because of the way it discretizes bathymetric slopes.

We find greater differences between the spectra of model and PCM-9 meridional velocity than between the spectra of zonal velocity. This we interpret as the model better representing planetary long waves than short waves. At the 50-day period, modeled and observed abyssal transport variability have low coherence because the model response to the long waves is inaccurate. The model reflects the long-wave energy mostly as a planetary short wave. In PCM-9 the energy is mostly lost along the Kermadec Ridge to a topographic wave with eastward (downslope) phase velocity. Spectra show that model and data both have a mixture of these waves but that the model favors the planetary wave whereas the observations favor the topographic wave. The zonal scales are different but are the same as the smaller and larger scales we see in PCM-9. We interpret this as evidence that the scales are set by planetary short waves for the larger, and topographic waves for the intense core of the DWBC which is confined to the ridge. In the case of the planetary wave scale, some balance must be struck between decay rate and zonal group speed.

Having found that the model represents planetary long waves well, we have used it to extend our view laterally, vertically, and in time. There are both long and short waves throughout the South Pacific at 32°S, with the amplitude of both increasing toward the west. The short-wave energy shows westward intensification approaching the East Pacific Rise, Kermadec Ridge, and Australia, consistent with the effects of wave reflection. The long-wave enhancement moving west is presumably associated with energy growth by continued generation as the waves propagate.

The complete vertical coverage of the model allows separation of barotropic and baroclinic components of the flow, which is not possible for the PCM-9 array design. East of the Kermadec Ridge there are baroclinic motions at semiannual and longer periods, and these correlate with the barotropic variability in such a way as to enhance surface energy and diminish abyssal energy (as would be necessary to meet a no-flow condition through the ridge). The baroclinic waves generated by this planetary wave scattering process propagate into the Tasman Sea and account for the increased semiannual period baroclinic energy there. The same process appears to occur at short periods in the region of $k-\omega$ space associated with barotropic planetary waves only. We assume the resulting baroclinic motions must be evanescent.

We are prompted to a final speculation on whether planetary waves, fundamental to the western boundary intensification of surface gyres, might play a similar role in the abyss. Since variability due to planetary waves clearly extends to abyssal depths, we might ask if some net pumping or retarding of the DWBC results, ultimately from the midlatitude atmospheric processes which force planetary waves?

From the data available to us, we can calculate a component of the Reynolds stress divergence, $-(\partial/\partial x)\langle u'v' \rangle$, which contributes to the mean meridional momentum balance. Below 2500 m in the model this term does not vary appreciably with depth and is largest immediately adjacent to the Kermadec Ridge, where it is directed southward at $0.7 \times 10^{-8} \text{ m s}^{-2}$. That is, it acts contrary to the direction of the DWBC. The term drops to zero over the model frictional boundary layer.

For PCM-9, Reynolds stress divergence is greatest at 2500 m between moorings 1 and 2, where it is directed northward at 10^{-7} m s^{-2} . Between the 2500 m instruments at moorings 3 and 5, it is $3 \times 10^{-8} \text{ m s}^{-2}$ southward. Deeper instruments give weaker values. The different character in these results calls their significance into question. However, the model's lack of a northward sense to $-(\partial/\partial x)\langle u'v' \rangle$ at the ridge might be expected given the absence, or at least underestimation, of northward momentum flux due to topographic waves. Further analysis is required to explore the possible interactions between the wave field and the mean DWBC. We note only that an acceleration of the order of 10^{-8} m s^{-2} , acting for 50 days, could drive a 4 cm s^{-1} mean flow; therefore its significance cannot be discounted.

We conclude that planetary waves are the dominant source of variability in the DWBC at periods of days to months. If variation in the deep-water formation processes is also a factor, it may well have its expression at much longer timescales. Certainly, it is not evident at seasonal timescales.

Acknowledgments. We thank colleagues L. Carter, J. Church, S. Godfrey, J. Pedlosky, and R. Pickart for discussions. The PCM-9 deployment was the work of T. Whitworth, B. Warren, W. Nowlin, and D. Pillsbury and their seagoing teams, and NIWA's CTD team and the crews of R/V *Rapuhia*, HMNZS *Monowai*, and FV *Giljanes*. PCM-9 was funded by the U.S. National Science Foundation. R. Smith and M. Maltrud at LANL kindly archived the special subset of model output at 32.5°S that made this study possible. J. Mansbridge prepared the model output for analysis. M.I.M. is supported by the New Zealand Foundation for Research Science and Technology. J.L.W. is funded by Australia's National Greenhouse Research Program. This work was made possible through NIWA's international collaboration program.

References

- Barnier, B., A numerical study on the influence of the Mid-Atlantic Ridge on nonlinear first-mode baroclinic Rossby waves generated by seasonal winds, *J. Phys. Oceanogr.*, 18, 417–433, 1988.
- Brillinger, D. R., Fourier analysis of stationary processes, *Proc. IEEE*, 62, 1628–1643, 1974.
- Chelton, D. B., and M. G. Schlax, Global observations of oceanic Rossby waves, *Science*, 272, 234–238, 1996.
- Dukowicz, J. K., and R. D. Smith, Implicit free-surface method for the Bryan-Cox-Semtner ocean model, *J. Geophys. Res.*, 99, 7991–8014, 1994.
- Gill, A. E., *Atmosphere-Ocean Dynamics*, 662 pp., Academic, San Diego, Calif., 1982.
- Jacobs, G. A., H. E. Hurlburt, J. C. Kindle, E. Metzger, J. L. Mitchell, W. Teague, and A. J. Wallcraft, Decade-scale trans-Pacific propagation and warming effects of an El Niño anomaly, *Nature*, 370, 360–363, 1994.
- Kiladis, G. N., G. A. Meehl, and K. M. Weickmann, Large-scale circulation associated with westerly wind bursts and deep convection over the western equatorial Pacific, *J. Geophys. Res.*, 99, 18,527–18,544, 1994.
- Koopmans, L. H., *The Spectral Analysis of Time Series*, 366 pp., Academic, San Diego, Calif., 1974.
- LeBlond, P. H., and L. A. Mysak, *Waves in the Ocean*, 602 pp., Elsevier, New York, 1978.
- Le Traon, P.-Y., and J.-F. Minster, Sea level variability and semiannual Rossby waves in the South Atlantic subtropical gyre, *J. Geophys. Res.*, 98, 12,315–12,326, 1993.
- McWilliams, J. C., and G. R. Flierl, Optimal, quasi-geostrophic wave analyses of MODE array data, *Deep Sea Res.*, 23, 285–300, 1976.
- Moore, M., CTD data from the southwest Pacific deep western boundary current: MAPKIWI-1, R/V *Rapuhia*, February–March 1991, *Tech. Rep. 94-5*, N. Z. Oceanogr. Inst., Wellington, 1994.
- Moore, M. I., and S. M. Chiswell, Countries collaborate on cruises, *WOCE Notes*, 5(3), 13–14, 1993.
- Moore, M. I., and P. Thomson, Impact of jittered sampling on con-

- ventional spectral estimates, *J. Geophys. Res.*, **96**, 18,519–18,526, 1991.
- Moore, M., S. M. Chiswell, and G. Knapp, CTD data from the southwest Pacific deep western boundary current: MAPKIWI-2, HMNZS *Monowai*, November–December 1992, *Tech. Rep. 93-2*, N. Z. Oceanogr. Inst., Wellington, 1993.
- Nowlin, W. D., Jr., and T. Whitworth III, PCM-9 deep western boundary current array deployed, *WOCE Newsl.*, **11**, 13, 1991.
- Pedlosky, J., A note on the western intensification of the oceanic circulation, *J. Mar. Res.*, **23**, 207–209, 1965.
- Pickart, R. S., and D. R. Watts, Deep western boundary current variability at Cape Hatteras, *Deep Sea Res.*, **48**, 765–791, 1990.
- Pillsbury, R., D. Barstow, J. Bottero, G. Pittock, D. Root, J. Simpkins III, R. Still, and T. Whitworth III, Deep western boundary currents in the southwestern Pacific Ocean, WOCE PCM-9 February 1991 to December 1992, *Tech. Rep. 94-3*, Coll. of Oceanic and Atmos. Sci., Oreg. State Univ., Corvallis, 1994.
- Price, J. F., and H. T. Rossby, Observations of a barotropic planetary wave in the western North Atlantic, *J. Mar. Res.*, **40**, suppl., 543–558, 1982.
- Priestley, M. B., *Spectral Analysis and Time Series*, 653 pp., Academic, San Diego, Calif., 1981.
- Reid, J., H. Stommel, E. D. Stroup, and B. Warren, Detection of a deep boundary current in the western South Pacific, *Nature*, **217**, 937, 1968.
- Roemmich, D. H., S. L. Hautala, and D. Rudnick, Northward abyssal transport through the Samoan Passage and adjacent regions, *J. Geophys. Res.*, **101**, 14,039–14,055, 1996.
- Stammer, D., R. Tokmakion, A. J. Semtner Jr., and C. Wunsch, How well does a $1/4^\circ$ global circulation model simulate large-scale oceanic observations, *J. Geophys. Res.*, **101**, 25,779–25,811, 1996.
- Stommel, H., and A. B. Arons, On the abyssal circulation of the world ocean, I, Stationary planetary flow patterns on a sphere, *Deep Sea Res.*, **6**, 140–154, 1960.
- Warren, B. A., General circulation of the South Pacific, in *Scientific Exploration of the South Pacific*, edited by W. S. Wooster, pp. 33–49, U.S. Natl. Acad. of Sci., Washington, D. C., 1970.
- Whitworth, T., III, B. A. Warren, and W. D. Nowlin Jr., Physical and chemical data from cruise 2041 of the R/V *Rapuhia* in the South Pacific Ocean, *Tech. Rep. 95-06-T*, Dep. of Oceanogr., Texas A&M Univ., College Station, 1995.
- M. I. Moore, New Zealand Dairy Board, P.O. Box 417, Wellington, NZ. (e-mail:moore@nzdb.co.nz)
- J. L. Wilkin, School of Environmental and Marine Sciences, University of Auckland, Tamaki Campus, Private Bay 92019, Auckland, NZ. (e-mail:john. Wilkin@marine. csiro.au)

(Received October 17, 1996; revised September 30, 1997;
accepted October 16, 1997.)